RSC Advances

PAPER

View Article Online
View Journal | View Issue

Cite this: *RSC Adv.*, 2023, **13**, 15457

Probing the physical properties of M_2LiCeF_6 (M = Rb and Cs) double perovskite compounds for prospective high-energy applications employing the DFT framework

Nasir Rahman, †*[a] Abdur Rauf,†[bc] Mudasser Husain,*[a] Nourreddine Sfina,[d] Vineet Tirth, [ef] Mohammad Sohail,[a] Rajwali Khan,[a] Ahmed Azzouz-Rached, [g] Ghulam Murtaza,[h] Abid Ali Khan,[i] Shaukat Ali Khattak [j] and Aurangzeb Khan[j]

Herein, the optoelectronic, structural, thermoelectric, and elastic characteristics of M_2LiCeF_6 (M = Rb and Cs) double perovskite compounds were investigated using *ab initio* modeling in the DFT framework. The Birch–Murnaghan fitting curve used for the optimization showed that these two compounds are structurally stable. The elastic properties of the M_2LiCeF_6 (M = Rb and Cs) double perovskite compounds were examined using the IRelast code. The results showed that these two compounds possess mechanical stability, anisotropy, and toughness, and offer resistance to plastic deformation. The precise and accurate determination of their electronic properties was achieved *via* the Trans-Blaha-modified Becke-Johnson (TB-mBJ) approximation. The Rb_2LiCeF_6 and Cs_2LiCeF_6 compounds are narrow band gap semiconductors with band gaps of 0.6 eV and 0.8 eV at the high symmetrical points from (Γ–M), respectively, exhibiting an indirect nature. To further understand how the various states contribute to the different band structures, total and partial density of state (DOS) computations were performed. The optical properties in the energy range of 0–40 eV for Rb_2LiCeF_6 and Cs_2LiCeF_6 were explored. The selected materials show transparency in the low incident photon energy range and have large light absorption and transmission at higher photon energies. Thus, it can be concluded that Rb_2LiCeF_6 and Cs_2LiCeF_6 can be used in high-frequency UV devices based on their optical characteristics. Both materials exhibit high electrical conductivity, power factors, and figures of merit (ZT) and act as effective thermoelectric resources. To the best of our knowledge, this is the first theoretical research on the optoelectronic, structural, thermoelectric, and elastic features of M_2LiCeF_6 (M = Rb and Cs).

Received 6th March 2023
Accepted 9th May 2023

DOI: 10.1039/d3ra01451g

rsc.li/rsc-advances

1. Introduction

Due to their exceptional stability, double perovskites (DPs), $A_2B'B''X_6$, can be applied in a variety of sustainable and renewable devices.[1–3] In recent years, exciting research on perovskite materials has been conducted in the fields of photovoltaics and photoluminescence.[4,5] Consequently, DPs have been widely implemented in optoelectronics[6–9] such as in solar cells[10,11]. As an alternative to $MAPBI_3$, the newly estimated Pb-free DPs are based on Ag and Bi, which are expected to be beneficial to the environment and have stability.[12–16] Currently, switching between organic and inorganic cations has increased the thermal stability of DPs.[17] In this context, many different substances have been tested, among which Pb-free DPs based on "Ag" and "In" are currently being explored. Various approaches have been employed to describe $Cs_2AgInCl_6$ for band gap calculations.[18–20] The next generation of photovoltaic technologies will benefit from the perovskites developed for

[a]*Department of Physics, University of Lakki Marwat, 28420, Lakki Marwat, KPK, Pakistan. E-mail: nasir@ulm.edu.pk; mudasserhusain01@gmial.com*
[b]*Institute for Advanced Study (IAS), Shenzhen University, Nanhai Avenue, Shenzhen 518060, Guangdong, P. R China*
[c]*College of Physics and Optoelectronics Engineering, Shenzhen University, Shenzhen 518060, Guangdong, P. R China*
[d]*College of Sciences and Arts in Mahayel Asir, Department of Physics, King Khalid University, Abha, Saudi Arabia*
[e]*Mechanical Engineering Department, College of Engineering, King Khalid University, Abha 61421, Kingdom of Saudi Arabia*
[f]*Research Center for Advanced Materials Science (RCAMS), King Khalid University, Guraiger, P.O. Box No. 9004, Abha 61413, Asir, Kingdom of Saudi Arabia*
[g]*Magnetic Materials Laboratory, Faculty of Exact Sciences, Djillali Liabes University of Sidi Bel-Abbes, Algeria*
[h]*Department of Physics, Islamia College University, Peshawar, KPK, Pakistan*
[i]*Department of Chemical Sciences, University of Lakki Marwat, 28420, Lakki Marwat, KPK, Pakistan*
[j]*Department of Physics, Abdul Wali Khan University, Mardan, KPK, Pakistan*
† These authors contributed equally to this work.

solar cells employing metal halide perovskites. Multi-junction solar cells have achieved a high power conversion efficiency (PCE), which has significantly increased over the last few years from 3.8% (ref. 21) to more than 24% according to the literature.[22,23] Recently, in 2019, multi-junction thin film solar cells attained a conversion efficiency of 47.1%.[24,25] The excellent performance of halide perovskites is attributed to their distinctive characteristics, including high charge carrier mobility, strong absorption, and direct and appropriate band gaps.[26–29] Halide double perovskites are constructed based on the physical characteristics of a variety of metal combinations. Cooling causes an octahedral tilt and increased electron–phonon interactions, which convert the potential cubic structure to a monoclinic structure. Halide perovskite semiconductors for transport and optoelectronic applications have been extensively explored despite their drawback of phase changes.[30,31] Organic or inorganic perovskites have suitable and stable photovoltaic (PV) properties and are widely applied in photoelectric devices.[32] PV systems are beneficial due to their non-polluting nature, gas-free carbon emissions, and abundant natural life compared to other types of perovskites.[33] However, their toxicity to humans and the environment is one of their major future limitations. Furthermore, their long-term instability on exposure to sunlight and atmospheric humidity is another challenge.[34,35] Perovskites have made significant advancements in thin-film devices such as photodetectors, lasers, and thin-film transistors. Numerous factors make perovskites a good choice for these types of devices. For example, perovskites can be created at low temperatures using dependable roll-to techniques for roll deposition.[36] Herein, DFT applied to WIEN2K and the BoltzTrap2 code was used to analyze the mechanical, optoelectronic, and thermoelectric properties of DPs. The computed results provide experimental researchers with guidelines and predictions for developing solar cell applications, which will help them find effective materials. Because of their superior structural, mechanical, and thermodynamic stability, the researched materials are exceptional for use in renewable energy applications. For the construction of devices, ductile behavior is crucial.

2. Computational details

DFT calculations using the full-potential linearized augmented plane wave plus local orbital (FPLAPW + lo) scheme utilized in the WIEN2K code were performed to screen the physical features of the materials.[37] For the investigation of the structural and elastic parameters at the ground state, the exchange-correlation interactions were considered through the GGA-PBE functional (generalized gradient approximation of Perdew Burke and Ernzerhof).[38] To compensate for the GGA-PBE functional underestimating the band gaps, the modified TB-mBJ potential was employed.[39] To gain insight into the electronic character of the materials, their electronic structure was computed. The extended spherical harmonic electronics in the wavefunction with l_{max} (maximum value of angular momentum) were set to 10 inside the muffin-tin sphere regimes. The wavefunctions were created on a plane wave basis set with a cut-off reciprocal lattice vector, K_{max}, equal to $10/R_{MT}^{min}$, where R_{MT}^{min} is the smallest muffin-tin sphere radius (RMT). To avoid overlapping spheres, the RMTs were chosen to be as large as possible, *i.e.*, $R_{MT}^{Rb} = 2.5$, $R_{MT}^{Li} = 1.67$, $R_{MT}{}^{Ce} = 2.17$, and $R_{MT}^{F} = 1.96$ Bohr. In an attempt to optimize the cell structure, more precise calculations with a higher cutoff energy and denser *k*-point sampling were carried out. The cutoff energy was raised to 41.2 Ry, and the irreducible Brillouin zone (IBZ) was considered in a 50 × 50 × 50 *k*-point mesh for the computation of the additional features (physical) that were considered, as well as 2000 Monkhorst–Pack *k*-points mesh for investigating the structural and other parameters.[40] To confirm the total energy converged to 10^{-5} Ry and that the force acting on each atom was less than 0.5 Ry Bohr^{-1}, the computational parameters were used. The equilibrium structural parameters, comprising the lattice parameter, were determined through the use of total energy minimization and internal coordinates. The elastic constants were computed utilizing the total energy *vs.* strain technique, as employed by Thomas Charpin[37] in the WIEN2K program. This method involved applying three different deformation types to the equilibrium lattice, including tetrahedral strain, hydrostatic stress, and rhombohedra strain, and then calculating the total energy changes consistent with the smeared deformations. The three single-crystal elastic constants, *i.e.*, C_{11}, C_{12}, and C_{44}, were the results for the cubic system. The dielectric function, $\varepsilon(\omega)$, which is related to the band gap found in the electronic structure, was the most crucial parameter to consider when analyzing the optical behavior of the materials. It was also necessary to derive relationships for the refractive index, $n(\omega)$, absorption and extinction coefficients, $I(\omega)$ and $K(\omega)$, respectively, energy loss function, $L(\omega)$, reflectivity $R(\omega)$, and optical conductivity, $\sigma(\omega)$. $\varepsilon(\omega)$ has real and imaginary components, *i.e.*, "$\varepsilon_1(\omega)$" and "ε_2 (ω)", respectively, in the form $\varepsilon(\omega) = \varepsilon_1(\omega) + i\varepsilon_2(\omega)$,[41] in which the imaginary component of the dielectric function represents the absorption of light by the material on its surface, while the real part represents the dispersion of light from the surface of the material.[42]

3. Results and discussion

3.1. Structural optimization

M_2LiCeF_6, where "M" is equal to Rb and Cs, crystallizes as a cubic perovskite with the $Fm\bar{3}m$ space group (#225). The M (M = Rb and Cs) atoms were shown to be at (0.25, 0.25, 0.75), Li atoms at (1/2, 0, 0), Ce atoms exists on (0, 0, 0) and F atoms at (0.26, 0, 0) and (0.25, 0, 0), respectively. Fig. 1 illustrates the cubic crystalline structure of the M_2LiCeF_6 (M = Rb and Cs) double perovskites. The optimized volume measured the structural parameters through the Birch–Murnaghan EoS.[43]

The calculated approximations of the evaluated points from the optimization curves depict the variation of volume *vs.* total energy and estimate the ground-state parameters, including the bulk modulus (B), pressure derivative of B (B'), and optimized lattice constant (a_0), and the minimum total energy of the unit cell with the corresponding volume, as presented in Fig. 2, will yield the unit cell with the lowest energy. In this section, the energy (total) was evaluated *vs.* unit cell volume (V_0).

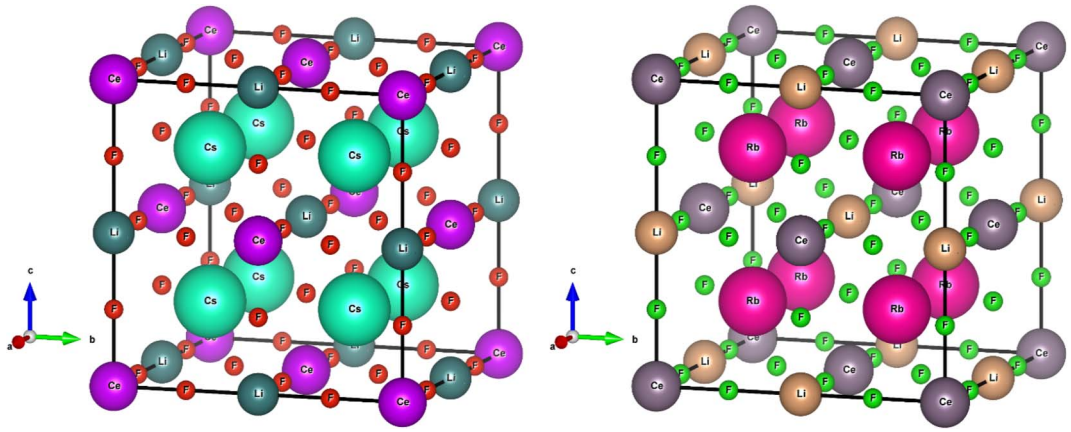

Fig. 1 Crystal unit cell of M_2LiCeF_6 (M = Rb and Cs) compounds. The atoms of the M (M = Rb and Cs) element are shown to be at (0.25, 0.25, 0.75), Li atoms at (1/2, 0, 0), Ce atoms at (0, 0, 0) and F atoms at (0.26, 0, 0) and (0.25, 0, 0), respectively.

The optimum energy, E_0, was obtained by plotting the total energy against volume, where the volume is denoted as V_0. The compound with the highest optimal energy is thought to have the most stable structure. The optimal structural data are shown in Table 1, including the equilibrium lattice constant (a_0), E_0, B_0, V_0, and B_0'. These findings are consistent with the overall pattern of this estimation because B is frequently reduced when a_0 is larger, indicating that the evaluated results are precise and useful.

3.2. Electronic properties

With the aim to analyze the electronic characteristics of the M_2LiCeF_6 (M = Rb and Cs) compounds, we investigated their real energy band structure, TDOS, and PDOS, as shown in Fig. 3. LDA and GGA calculations often find that the band gap (fundamental) between a semiconductor and insulator is underestimated.[44,45] Generally, this is due to the fact that the exchange-correlation energies and charges derivative cannot be consistently generated by their fundamental geometries. Thus, the TB-mBJ approximation was successfully used in some recent studies to correct the underestimated troublesome band gaps.[46–49] The optimal geometries of the M_2LiCeF_6 (M = Rb and Cs) compounds with assessed energy band structures over larger symmetries are displayed in Fig. 3a and b, respectively.

The band gaps of Rb_2LiCeF_6 and Cs_2LiCeF_6 in TB-MBJ are 0.6 eV and 0.8 eV, respectively, with an indirect band gap along the Γ–X points of symmetry. The conduction band maxima are flat and move from Γ–X, confirming the narrow-band semiconducting nature of both compounds. To gain a thorough understanding, the TDOS, PDOS and band structures were examined, and their spectra are shown in Fig. 3a and b in the energy range of −14 eV to 8 eV. The role of the electronic states in the VB and CB is displayed in the DOS plots. The Fermi energy level (E_F), as illustrated by the vertical dashed line at 0 eV, is used to indicate the DOS in the energy range of −14 eV to 8 eV. The part above E_F shows the VB, whereas that below specifies the CB. In the case pf Rb_2LiCeF_6, the energy range is split into two groups based on the PDOS distribution, with the energy range of $BaCuF_3$ being 0 eV to 0.8 eV (VB) and 0 eV to −6.8 eV (CB), while that for Cs_2LiCeF_6 is 0 eV to 1 eV (VB) and 0 eV to −5.5 eV, respectively. The band structure and narrow band gap semiconducting properties of these compounds are supported by the DOS plots. The "Rb" atom, as shown in red,

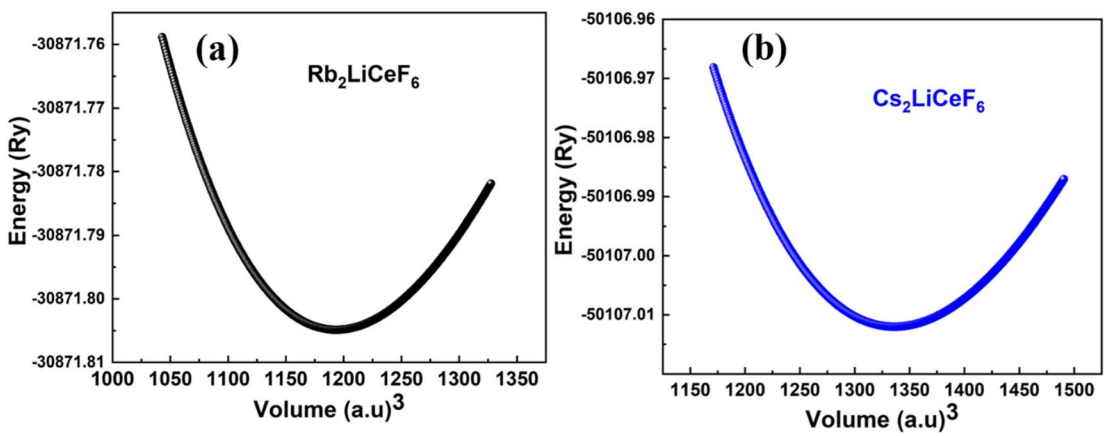

Fig. 2 Energy *vs.* volume plots of M_2LiCeF_6 (M = Rb and Cs) compounds.

Table 1 Parameters of the M_2LiCeF_6 (M = Rb and Cs) ternary compound crystal unit cell that were tuned structurally. E_0 in Ry, B_0 and B_0' in GPa, and the lattice constant a_0 in Å

Structural specifications	Rb_2LiCeF_6	Cs_2LiCeF_6
a_0 (Å)	8.91	9.25
V_0 (a.u^3)	1193.70	1336.21
B_0 (GPa)	55.20	50.11
B_0' (GPa)	4.72	4.37
E_0 (Ry)	−3087.80	−50107.01

makes up the majority of the density of states in the VB for Rb_2LiCeF_6, whereas the Ce atom, as shown in blue, makes up the majority of the density of states in CB. In contrast, for Cs_2LiCeF_6, the Li atom, as shown in green in the VB, and the Ce atom, as shown as blue in the CB, both contribute significantly to the density of states.

3.3. Elastic properties

To predict the mechanical parameters of materials, EC (elastic constant) is significant and determines how crystals respond to stimuli. The hardness and stability of a material can be evaluated using the measured EC. In this case, examining the EC of a material under zero pressure involves calculating the tensor and stress characteristics for very small strains as well as employing energy to track the lattice strains that persist to the volume.[50] The IRelast package, incorporated in WIEN2K developed chiefly for cubic structures, was used to compute the ECs. Only three ECs, *i.e.*, C_{11}, C_{12}, and C_{44}, were utilized in place of C_{ij} owing to the cubic lattice symmetry. Table 2 presents the computed ECs used to produce the assessed ECs and other elastic property characteristics. The cubic crystal mechanical stability criteria, which place restrictions on the elastic constants, are $C_{11} > 0$, $C_{44} > 0$, $C_{11} - C_{12} > 0$, $C_{11} + 2C_{12} > 0$, and $B > 0$. These stability requirements show how elastic stability is present in particular materials.

Rb_2LiCeF_6 has a C_{11} value of 104.11 GPa compared to that of Cs_2LiCeF_6 of 98.97 GPa, demonstrating a minor hardness advantage for Rb_2LiCeF_6. The parameter "A" of the crystal, which is critical in engineering research, is closely related to the propensity of a material to produce microcracks.

$$A = 2C_{44}/(C_{11} - C_{12}) \quad (1)$$

For fully isotropic materials, $A = 1$, whereas any value below or above "1" denotes anisotropy. Here, both compounds are anisotropic given that "*A*" varies between "1" and 1.5, and the degree of anisotropy is constrained by the level of variation. As

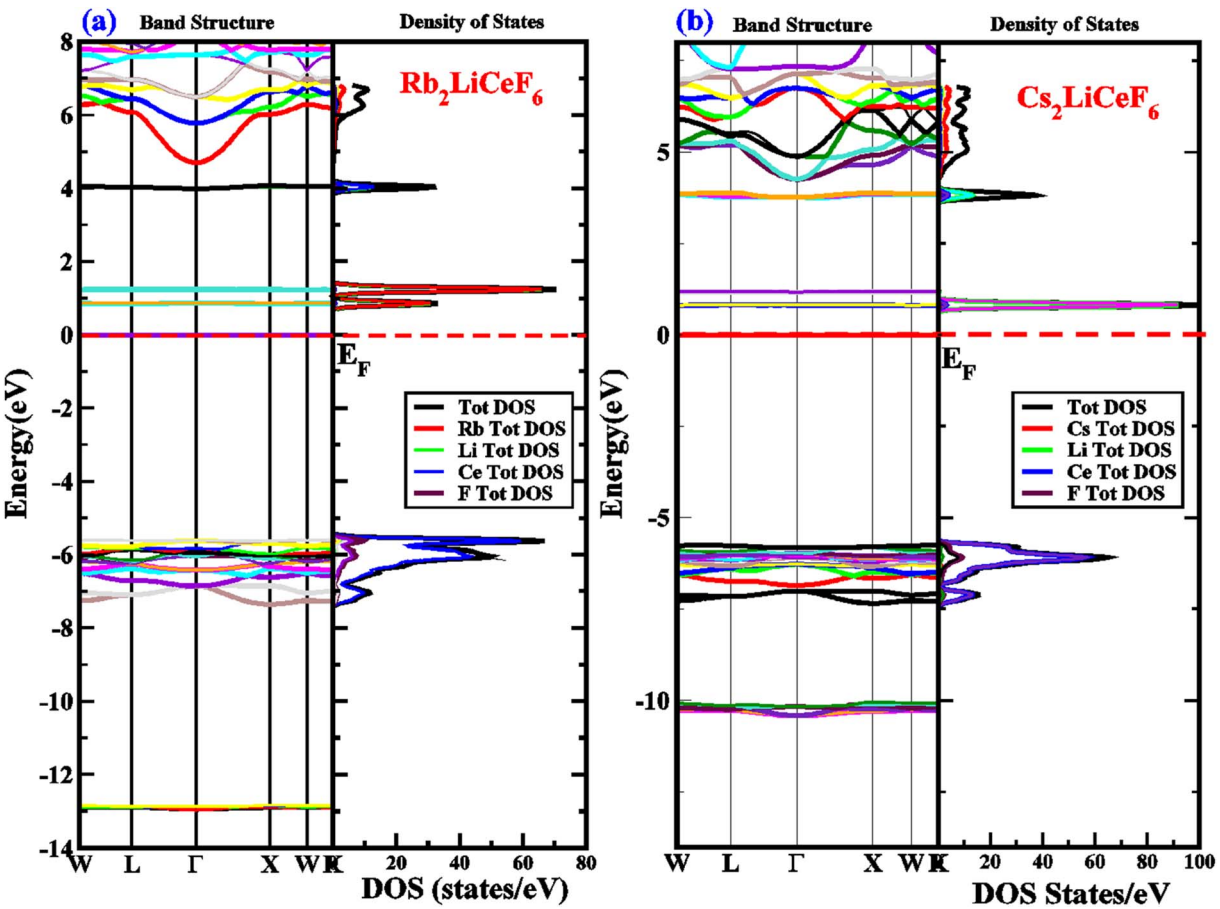

Fig. 3 (a) and (b) Electronic energy bands structure and DOS of M_2LiCeF_6 (M = Rb and Cs) compounds using TB-mBJ approximation, respectively.

Table 2 Investigated parameters of elastic properties, which include EC (elastic constant), B (bulk modulus), anisotropy factor (A), Young's modulus (E), Poisson's ratio (ν), Pugh ratio (B/G), B/C_{44}, $C_{11}-C_{12}$, shear modulus (G), and $C_{11}-C_{44}$ for Rb_2LiCeF_6 and Cs_2LiCeF_6 quaternary double perovskites compounds

Elastic parameter	Rb_2LiCeF_6	Cs_2LiCeF_6
C_{11} (GPa)	104.11	98.97
C_{12} (GPa)	32.79	26.48
C_{44} (GPa)	20.36	44.64
B (GPa)	56.69	50.70
A	0.57	1.23
E (GPa)	68.74	97.42
ν	0.29	0.27
B/G	2.22	1.89
B/C_{44}	2.78	1.13
$C_{11}-C_{12}$ (GPa)	75.43	47.82
G (GPa)	7.18	7.79
$C_{11}-C_{44}$ (GPa)	111.43	95.4

can be observed from the examined values of A for Rb_2LiCeF_6 (0.57) and Cs_2LiCeF_6 (1.23), both of these compounds display a significant amount of anisotropy. Subsequently, it was necessary to compute the other elastic components, *i.e.*, G, E, and ν, employing the elastic constants and the equations below.[51,52]

$$E = \frac{9GB}{3B+G} \quad (2)$$

$$\nu = \frac{3B-2G}{2(3B+G)} \quad (3)$$

$$G_V = \frac{1}{5}(C_{11}-C_{12}+3C_{44}) \quad (4)$$

$$G_R = \frac{5C_{44}(C_{11}-C_{12})}{4C_{44}+3(C_{11}-C_{12})} \quad (5)$$

The results of applying the aforementioned equations to determine the values of A, E, ν, and G are displayed in Table 2. The Cauchy pressure is represented as $C_{11}-C_{44}$, which serves to identify ductile materials.[53] If $C_{11}-C_{44}$ is positive, the materials exhibit a ductile nature, whereas if it is negative, the materials will be brittle. The positive Cauchy pressure values of 83.75 GPa for Rb_2LiCeF_6 and 54.33 GPa for Cs_2LiCeF_6 indicate their ductile character. Another way to determine brittleness or ductility is the Pugh ratio (B/G). Materials are thought to be more ductile if their B/G ratio is high, which must be greater than 1.75.[54] The critical points in this study were different for both compounds, which were 2.22 for Rb_2LiCeF_6 and 1.89 for Cs_2LiCeF_6. By using "ν" to distinguish between the ductility and brittleness of the material, Frantsevich *et al.*[55] discovered that a critical value of 0.26 was mandatory. Brittle materials have values below 0.26, whereas ductile materials have values over 0.26. Based on the value of 0.29 for Rb_2LiCeF_6 and 0.27 for Cs_2LiCeF_6, both of compounds are ductile in nature, as demonstrated in Table 2. The corresponding material has great lubricating capabilities if B/C_{44} has large values. Young's modulus (Y) and the values of ($C_{11}-C_{12}$) can also be used for evaluating plasticity. Greater flexibility of interested compounds is shown by lower values of ($C_{11}-C_{12}$) and "Y". Thus, the Rb_2LiCeF_6 and Cs_2LiCeF_6 compounds have mechanical stability, anisotropy, toughness, strength, and good crack resistance.

3.4. Optical properties

To examine all the optical properties, the theoretical equilibrium lattice constants were used, *i.e.*, $\varepsilon(\omega)$ was examined.

3.4.1. Dielectric function. The computed real part, $\varepsilon_1(\omega)$, for both materials is shown in Fig. 4a, and the imaginary portion, $\varepsilon_2(\omega)$, is shown in Fig. 4b for the incident photon energy range of up to 40 eV. In contrast to the imaginary part, $\varepsilon_2(\omega)$, which is related to the polarization and is responsible for the capacity of a material to store energy, $\varepsilon_1(\omega)$ defines the energy dissipation and wave damping. The predicted static dielectric function, $\varepsilon_1(0)$, for both materials is shown in Fig. 4a, which shows that Rb_2LiCeF_6 wastes more energy than Cs_2LiCeF_6, with $\varepsilon_1(0)=3.6$ for Rb_2LiCeF_6 and 3.4 for Cs_2LiCeF_6. The Penn model predicts that materials possessing higher band gaps have low $\varepsilon_1(0)$ and *vice versa*. The results show that these materials adhere to the Penn model. The figure illustrates $\varepsilon_2(\omega)$, which depicts the polarizability of a material, as shown in Fig. 4b. No polarization was present in either material at an incident photon energy of 0 eV.

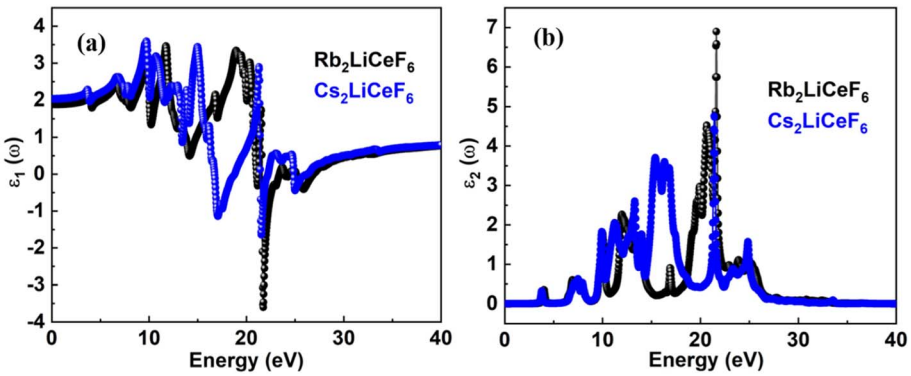

Fig. 4 $\varepsilon_1(\omega)$ and $\varepsilon_2(\omega)$ for (a) Rb_2LiCeF_6 and (b) Cs_2LiCeF_6.

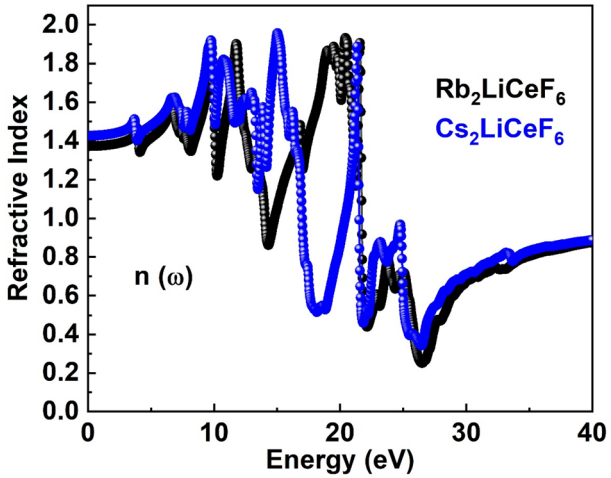

Fig. 5 $n(\omega)$ of M_2LiCeF_6 (M = Rb and Cs) compounds.

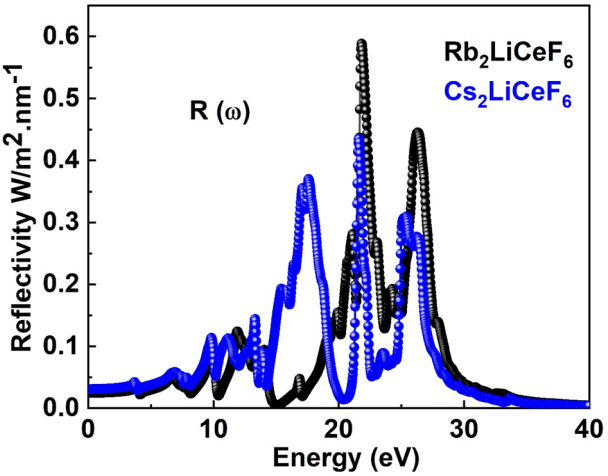

Fig. 7 $R(\omega)$ of M_2LiCeF_6 (M = Rb and Cs) compounds.

3.4.2. Refractive index. $\sigma(\omega)$, $I(\omega)$, and $R(\omega)$ can be computed using the $\varepsilon_1(\omega)$ and $\varepsilon_2(\omega)$ of the refractive index. The examined $n(\omega)$ is illustrated in Fig. 5. The spectrum of $n(\omega)$ for Rb_2LiCeF_6 and Cs_2LiCeF_6 each has a static refractive index, $n(0)$, of 1.4 and 1.42, respectively. The peak value of $n(\omega)$ for Cs_2LiCeF_6 is 1.92 at approximately 15 eV and Rb_2LiCeF_6 has a maximum peak $n(\omega)$ of 1.9 at approximately 20 eV photon energy. To calculate the light refraction, the statistic refractive index, $n(\omega)$, is helpful, especially in photoelectric applications. Given that $n(\omega)$ >1 because of the reduction in the speed of photons when they enter matter, they interact with the electrons. More photons are delayed when they pass through a substance with a higher $n(\omega)$. Every technique that increases the electronic density of a material also increases its $n(\omega)$.

3.4.3. Absorption coefficient. Fig. 6 displays the $I(\omega)$ curves obtained using the $\varepsilon(\omega)$ approach. Fig. 6 shows that the chosen compounds have a significant $I(\omega)$ at energies between 0 eV and 40 eV.

The threshold point of Rb_2LiCeF_6 and Cs_2LiCeF_6 is 0 eV, which is the point where these substances begin to absorb electromagnetic radiation. At the photon energy of 22 eV, Rb_2LiCeF_6 has a maximum absorption of 490, whereas that of Cs_2LiCeF_6 is 370.44.

3.4.4. Reflectivity. The computed $R(\omega)$ for both double perovskites compounds is depicted in Fig. 7. Rb_2LiCeF_6 has a zero-frequency $R(0)$ of 0.03, while Cs_2LiCeF_6 possesses a value of 0.02, and with an increase in photon energy, their reflectivity increases to a maximum of 0.59 and 0.43 at about 23 eV, respectively.

Thus, these materials have a very low reflectivity in the measured energy range, which is consistent with their band gap, making them transparent to incoming photons. Consequently, they can be applied in solar cells and lenses.

3.4.5. Optical conductivity. With the application of an electromagnetic field, electrons behave in a manner known as $\sigma(\omega)$. The outcome of assessing $\sigma(\omega)$ using dielectric functions is depicted in Fig. 8.

According to Fig. 8, the optical conductivity, $\sigma(\omega)$, of the materials starts to develop close to their band gap energy, which

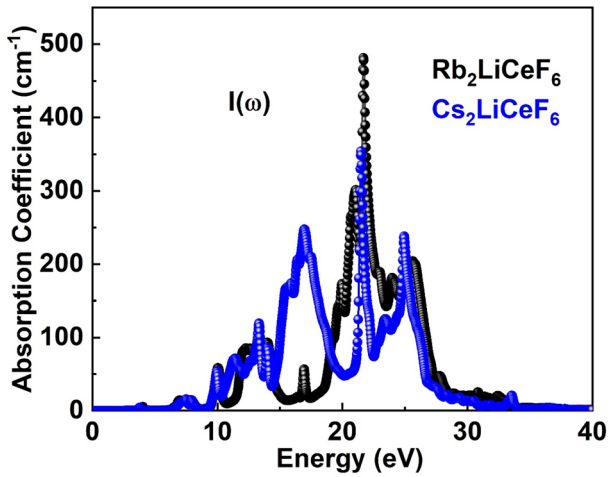

Fig. 6 $I(\omega)$ of M_2LiCeF_6 (M = Rb and Cs) compounds.

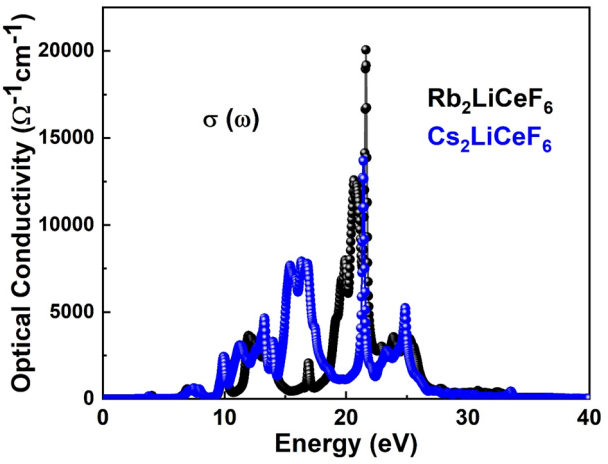

Fig. 8 $\sigma(\omega)$ of M_2LiCeF_6 (M = Rb and Cs) compounds.

is between 8–10 eV. In contrast to Rb_2LiCeF_6, which has a maximum $\sigma(\omega)$ of about 20 000 Ω^{-1} cm^{-1}, the Cs_2LiCeF_6 compound has a major $\sigma(\omega)$ of about 12 500 Ω^{-1} cm^{-1}, as seen in Fig. 8. Thus, as a result of their excellent optical conductivity at high energies, these compounds may find application in numerous contemporary optoelectronic devices.

3.5. Thermoelectric properties

The Rb_2LiCeF_6 and Cs_2LiCeF_6 compounds are thought to exhibit strong thermoelectric capabilities because of their high estimated band gap energy and electronic state degeneracy. The transport properties of the Rb_2LiCeF_6 and Cs_2LiCeF_6 compounds *vs.* temperature are described in detail and the computed spectra of several parameters are shown in Fig. 9–12.

3.5.1. Seebeck coefficient "*S*". Fig. 9 displays the estimated "*S*" for the M_2LiCeF_6 (M = Rb and Cs) compounds.

The emergence of an electric potential through a temperature gradient in various electrical conductors or semiconductors is known as the Seebeck effect. Based on the concentration of charge carriers, the value of "*S*" was computed starting roughly at 100 K, which for both compounds increased exponentially with temperature, reaching a maximum of 90 V K^{-1} for Rb_2LiCeF_6 and 94 V K^{-1} for Cs_2LiCeF_6. The fact that both compounds have positive "*S*" values demonstrates that they are p-type compounds, making them active thermoelectric materials at higher temperatures. The greater size of the hole effective mass is the reason why the Seebeck coefficient (S) for p-type is higher than for n-type throughout the whole range of selected carrier concentrations.

3.5.2. Thermal power factor (PF). The PF ($S^2\sigma/\tau$) for both compounds was plotted against relaxation time, as shown in. Fig. 10. PF is denoted by the term "$S^2\sigma$" in the expression for "ZT". Rb_2LiCeF_6 has a maximum "PF" value of 1×10^{11} W mK^{-2} s, while that of Cs_2LiCeF_6 reaches 6.5×10^{11} W mK^2 s at around 850 K. Due to its higher "$S^2\sigma$" value, Cs_2LiCeF_6 is anticipated to have stronger thermoelectric capabilities than

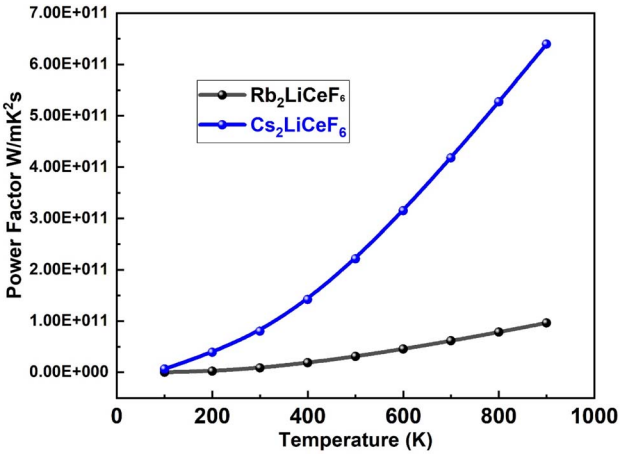

Fig. 10 Power factor "PF" *vs.* temperature for M_2LiCeF_6 (M = Rb and Cs) compounds.

Rb_2LiCeF_6 at high temperatures. Although it is frequently asserted that thermoelectric (TE) devices made of materials with higher power factors can 'generate' more energy (move more heat or extract more energy from the temperature difference), this can be only true for a thermoelectric device with fixed geometry and an unlimited heat source and cooling.

3.5.3. Thermal conductivity. Fig. 11 displays the investigated thermal conductivity *versus* temperature of Rb_2LiCeF_6 and Cs_2LiCeF_6. Low thermal conductivity and maximum electric carrier transport are characteristics of good thermoelectric materials. For many technological and temperature-critical applications, such as materials for thermoelectric conversion and thermal barrier coatings with higher temperature capabilities, thermal conductivity is an important parameter in the identification and development of alternative materials.

Good thermoelectric behavior is shown by the linear increase in thermal conductivity at low temperatures as the temperature increases. Rb_2LiCeF_6 is a suitable thermoelectric material

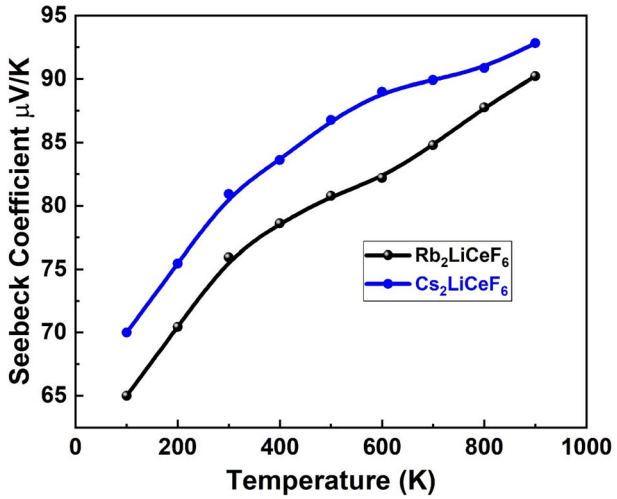

Fig. 9 Seebeck coefficient *vs.* temperature for M_2LiCeF_6 (M = Rb and Cs) compounds.

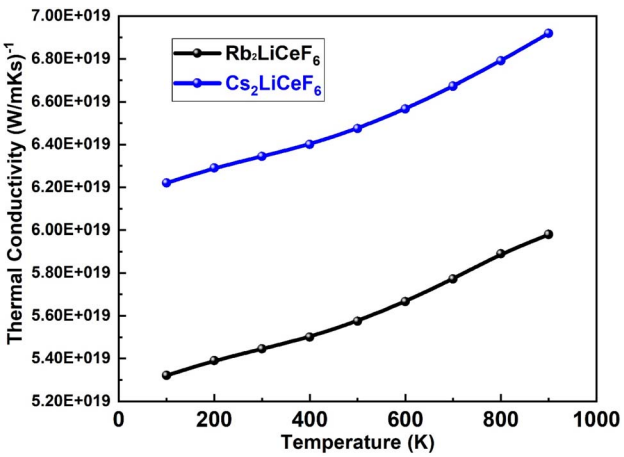

Fig. 11 Thermal conductivity *vs.* temperature of M_2LiCeF_6 (M = Rb and Cs) compounds.

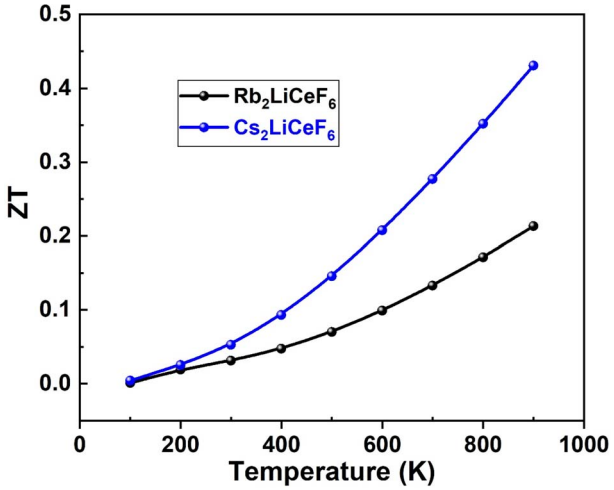

Fig. 12 Figure-of-merit "*ZT*" *vs.* temperature of Rb_2LiCeF_6 and Cs_2LiCeF_6.

because its thermal conductivity values are lower than that of Cs_2LiCeF_6.

3.5.4. Figure of merit "*ZT*". The dimensionless parameter "*ZT*" is used to rate thermoelectric materials and is significant for the quality of a material. As the "*ZT*" value increases, the thermoelectric efficiency, *i.e.*, the heat conversion to electricity, increases. The formula for the figure-of-merit is $ZT = S^2\sigma T/\lambda$, where $S^2\sigma$ is the PF in the numerator. The highest value of "*ZT*" for an ideal thermoelectric material is 1, and thus achieving a value of "*ZT*" of ~1 is the goal of materials scientists. Fig. 12 illustrates the greatest values of "*ZT*" achieved for Rb_2LiCeF_6 and Cs_2LiCeF_6 in this scenario, which were 0.20 and 0.45, respectively, demonstrating that they are both effective thermoelectric materials.

These findings imply that the compounds under investigation possess intriguing thermoelectric capabilities and that Cs_2LiCeF_6 exhibits superior thermoelectric properties to Rb_2LiCeF_6.

4. Conclusion

Using the WIEN2K and BoltzTrap2 codes, the elastic, structural, optoelectronic, and thermoelectric features of M_2LiCeF_6 (M = Rb and Cs) double perovskites were examined computationally. Based on the results of some physical properties, the following conclusions were drawn.

Both M_2LiCeF_6 (M = Rb and Cs) double perovskites crystallize as stable cubic structures. M_2LiCeF_6 (M = Rb and Cs) exhibits an indirect band gap along the (Γ–X) symmetry points, which depicts that both materials are semiconductors. According to the DOS report, the Rb element dominates the contribution of the states in the band structures in the valence bands and the Ce atom in the conduction band for Rb_2LiCeF_6, whereas the Li element contributes more in the valence bands and Ce contributes in the CB for Cs_2LiCeF_6. The mechanical properties of the M_2LiCeF_6 (M = Rb and Cs) double perovskites reveal that these compounds are ductile, anisotropic, and elastically stable. The optical characteristics for incident photon energies are in the range of 0–40 eV. These materials can be active compounds in photovoltaic and optoelectronic devices because of their estimated maximum optical conductivity and absorption at a higher energy of incident photons. In addition, these compounds possess a considerably high "*S*" and "*ZT*" (figure of merit), signifying their prospective thermoelectric applications.

Conflicts of interest

There are no conflicts of interest to declare.

Acknowledgements

The authors extend their appreciation to the Deanship of Scientific Research at King Khalid University (Abha, Saudi Arabia) for funding this work through Research Groups Program under grant number (RGP.2/379/44).

References

1 G. Li, *et al.*, Near-infrared responsive Z-scheme heterojunction with strong stability and ultra-high quantum efficiency constructed by lanthanide-doped glass, *Appl. Catal., B*, 2022, **311**, 121363.
2 F. Igbari, Z. Wang and L. Liao, Progress of lead-free halide double perovskites, *Adv. Energy Mater.*, 2019, **9**(12), 1803150.
3 X.-G. Zhao, D. Yang, J.-C. Ren, Y. Sun, Z. Xiao and L. Zhang, Rational design of halide double perovskites for optoelectronic applications, *Joule*, 2018, **2**(9), 1662–1673.
4 H. Wang, *et al.*, Interface engineering with a novel n-type small organic molecule for efficient inverted perovskite solar cells, *Chem. Eng. J.*, 2020, **392**, 123677.
5 Q. A. Akkerman, *et al.*, Tuning the optical properties of cesium lead halide perovskite nanocrystals by anion exchange reactions, *J. Am. Chem. Soc.*, 2015, **137**(32), 10276–10281.
6 X. Li, Q. Kong, X. An, J. Zhang, Q. Wang and W. Yao, Enhanced cycling stability and storage performance of Na0. 67Ni0. 33Mn0. 67-xTixO1. 9F0. 1 cathode materials by Mn-rich shells and Ti doping, *J. Colloid Interface Sci.*, 2023, **633**, 82–91.
7 L. C. Schmidt, *et al.*, Nontemplate synthesis of CH3NH3PbBr3 perovskite nanoparticles, *J. Am. Chem. Soc.*, 2014, **136**(3), 850–853.
8 D. P. McMeekin, *et al.*, A mixed-cation lead mixed-halide perovskite absorber for tandem solar cells, *Science*, 2016, **351**(6269), 151–155.
9 J. Chen, M. E. Messing, K. Zheng and T. Pullerits, Cation-dependent hot carrier cooling in halide perovskite nanocrystals, *J. Am. Chem. Soc.*, 2019, **141**(8), 3532–3540.
10 Y. S. Park, S. Guo, N. S. Makarov and V. I. Klimov, Room temperature single-photon emission from individual perovskite quantum dots, *ACS Nano*, 2015, **9**, 10386–10393.
11 J. Liu, J. Leng, K. Wu, J. Zhang and S. Jin, Observation of internal photoinduced electron and hole separation in

hybrid two-dimensional perovskite films, *J. Am. Chem. Soc.*, 2017, **139**(4), 1432–1435.

12 Y. Wei, *et al.*, High-Performance Visible to Near-Infrared Broadband Bi2O2Se Nanoribbon Photodetectors, *Adv. Opt. Mater.*, 2022, **10**(23), 2201396.

13 X. Chen, C. Wang, Z. Li, Z. Hou and W.-J. Yin, Bayesian optimization based on a unified figure of merit for accelerated materials screening: A case study of halide perovskites, *Sci. China Mater.*, 2020, **63**(6), 1024–1035.

14 A. H. Slavney, T. Hu, A. M. Lindenberg and H. I. Karunadasa, A bismuth-halide double perovskite with long carrier recombination lifetime for photovoltaic applications, *J. Am. Chem. Soc.*, 2016, **138**(7), 2138–2141.

15 E. T. McClure, M. R. Ball, W. Windl and P. M. Woodward, Cs2AgBiX6 (X= Br, Cl): new visible light absorbing, lead-free halide perovskite semiconductors, *Chem. Mater.*, 2016, **28**(5), 1348–1354.

16 M. R. Filip, S. Hillman, A. A. Haghighirad, H. J. Snaith and F. Giustino, Band gaps of the lead-free halide double perovskites Cs2BiAgCl6 and Cs2BiAgBr6 from theory and experiment, *J. Phys. Chem. Lett.*, 2016, **7**(13), 2579–2585.

17 R. J. Sutton, *et al.*, Bandgap-tunable cesium lead halide perovskites with high thermal stability for efficient solar cells, *Adv. Energy Mater.*, 2016, **6**(8), 1502458.

18 M. Fu, W. Chen, Y. Lei, H. Yu, Y. Lin and M. Terrones, Biomimetic Construction of Ferrite Quantum Dot/Graphene Heterostructure for Enhancing Ion/charge Transfer in Supercapacitors, *Adv. Mater.*, 2023, 2300940.

19 T. T. Tran, J. R. Panella, J. R. Chamorro, J. R. Morey and T. M. McQueen, Designing indirect–direct bandgap transitions in double perovskites, *Mater. Horiz.*, 2017, **4**(4), 688–693.

20 J. Luo, *et al.*, Efficient and stable emission of warm-white light from lead-free halide double perovskites, *Nature*, 2018, **563**(7732), 541–545.

21 A. Kojima, K. Teshima, Y. Shirai and T. Miyasaka, Organometal halide perovskites as visible-light sensitizers for photovoltaic cells, *J. Am. Chem. Soc.*, 2009, **131**(17), 6050–6051.

22 L. Shi, *et al.*, Accelerated lifetime testing of organic–inorganic perovskite solar cells encapsulated by polyisobutylene, *ACS Appl. Mater. Interfaces*, 2017, **9**(30), 25073–25081.

23 W. S. Yang, *et al.*, High-performance photovoltaic perovskite layers fabricated through intramolecular exchange, *Science*, 2015, **348**(6240), 1234–1237.

24 C. Han, H. Wang, Z. Wang, X. Ou and Y. Tang, Solvation Structure Modulation Of High-Voltage Electrolyte For High-Performance K-Based Dual-Graphite Battery, *Adv. Mater.*, 2013, 2300917.

25 J. F. Geisz, M. A. Steiner, K. L. Schulte, M. Young, R. M. France and D. J. Friedman, Six-junction concentrator solar cells, *AIP Conf. Proc.*, 2018, **2012**(1), 40004.

26 J. H. Noh, S. H. Im, J. H. Heo, T. N. Mandal and S. Il Seok, Chemical management for colorful, efficient, and stable inorganic–organic hybrid nanostructured solar cells, *Nano Lett.*, 2013, **13**(4), 1764–1769.

27 S. D. Stranks, *et al.*, Electron-hole diffusion lengths exceeding 1 micrometer in an organometal trihalide perovskite absorber, *Science*, 2013, **342**(6156), 341–344.

28 Q. Dong, *et al.*, Electron-hole diffusion lengths> 175 μm in solution-grown CH3NH3PbI3 single crystals, *Science*, 2015, **347**(6225), 967–970.

29 D. Shi, *et al.*, Low trap-state density and long carrier diffusion in organolead trihalide perovskite single crystals, *Science*, 2015, **347**(6221), 519–522.

30 M. Wang, C. Jiang, S. Zhang, X. Song, Y. Tang and H.-M. Cheng, Reversible calcium alloying enables a practical room-temperature rechargeable calcium-ion battery with a high discharge voltage, *Nat. Chem.*, 2018, **10**(6), 667–672.

31 A. E. Maughan, A. M. Ganose, M. A. Almaker, D. O. Scanlon and J. R. Neilson, Tolerance factor and cooperative tilting effects in vacancy-ordered double perovskite halides, *Chem. Mater.*, 2018, **30**(11), 3909–3919.

32 M. M. Lee, J. Teuscher, T. Miyasaka, T. N. Murakami and H. J. Snaith, Efficient hybrid solar cells based on meso-superstructured organometal halide perovskites, *Science*, 2012, **338**(6107), 643–647.

33 T. Kirchartz, J. Bisquert, I. Mora-Sero and G. Garcia-Belmonte, Classification of solar cells according to mechanisms of charge separation and charge collection, *Phys. Chem. Chem. Phys.*, 2015, **17**(6), 4007–4014.

34 X. Zhang, Y. Tang, F. Zhang and C. Lee, A novel aluminum–graphite dual-ion battery, *Adv. Energy Mater.*, 2016, **6**(11), 1502588.

35 N. J. Jeon, *et al.*, Compositional engineering of perovskite materials for high-performance solar cells, *Nature*, 2015, **517**(7535), 476–480.

36 F. Di Giacomo, A. Fakharuddin, R. Jose and T. M. Brown, Progress, challenges and perspectives in flexible perovskite solar cells, *Energy Environ. Sci.*, 2016, **9**(10), 3007–3035.

37 T. Charpin, *A Package for Calculating Elastic Tensors of Cubic Phase Using WIEN*, Laboratory of Geometrix, Paris, 2001.

38 P. Blaha, K. Schwarz, G. K. H. Madsen, D. Kvasnicka, and J. Luitz, *wien2k," An Augment. Pl. wave+ local orbitals Progr. Calc. Cryst. Prop.*, vol. 60, 2001.

39 J. P. Perdew, K. Burke and M. Ernzerhof, Generalized gradient approximation made simple, *Phys. Rev. Lett.*, 1996, **77**(18), 3865.

40 F. Tran and P. Blaha, Accurate band gaps of semiconductors and insulators with a semilocal exchange-correlation potential, *Phys. Rev. Lett.*, 2009, **102**(22), 226401.

41 S. Saha, T. P. Sinha and A. Mookerjee, Electronic structure, chemical bonding, and optical properties of paraelectric $BaTiO_3$, *Phys. Rev. B*, 2000, **62**(13), 8828–8834.

42 M. Husain, *et al.*, Exploring the exemplary structural, electronic, optical, and elastic nature of inorganic ternary cubic $XBaF_3$ (X = Al and Tl) employing the accurate TB-mBJ approach, *Semicond. Sci. Technol.*, 2022, **37**(7), 075004.

43 F. D. Murnaghan, The compressibility of media under extreme pressures, *Proc. Natl. Acad. Sci. U. S. A.*, 1944, **30**(9), 244.

44 P. Dufek, P. Blaha and K. Schwarz, Applications of Engel and Vosko's generalized gradient approximation in solids, *Phys. Rev. B: Condens. Matter Mater. Phys.*, 1994, **50**(11), 7279.

45 Z. Charifi, H. Baaziz, F. E. H. Hassan and N. Bouarissa, High pressure study of structural and electronic properties of calcium chalcogenides, *J. Phys.: Condens. Matter*, 2005, **17**(26), 4083.

46 N. Rahman, *et al.*, First principle study of structural, electronic, optical and mechanical properties of cubic fluoro-perovskites:(CdXF3, X= Y, Bi), *Eur. Phys. J. Plus*, 2021, **136**(3), 1–11.

47 M. Sohail, *et al.*, First-principal investigations of electronic, structural, elastic and optical properties of the fluoroperovskite TlLF 3 (L= Ca, Cd) compounds for optoelectronic applications, *RSC Adv.*, 2022, **12**(12), 7002–7008.

48 M. A. Ali, *et al.*, A theoretical study of the structural, hermoelectric, and spin-orbit coupling influenced optoelectronic properties of CsTmCl3 halide perovskite, *Int. J. Quantum Chem.*, 2020, **120**(7), e26141.

49 A. Mohamed, A. El Houssine, F. Nejmaa, and B. Ibrahim, Ab-initio Study of Electronic, Optical and Thermoelectric properties of TiO2 phases using mBJ approximation, in *2020 IEEE 6th International Conference on Optimization and Applications*, ICOA, 2020, pp. 1–5.

50 M. J. Mehl, Pressure dependence of the elastic moduli in aluminum-rich Al-Li compounds, *Phys. Rev. B: Condens. Matter Mater. Phys.*, 1993, **47**(5), 2493.

51 R. Hill, The elastic behaviour of a crystalline aggregate, *Proc. Phys. Soc. A*, 1952, **65**(5), 349.

52 W. Voigt, *Lehrbuch der Kristallphysik (Textbook of crystal physics)*, BG Teubner, Leipzig und Berlin, 1928.

53 D. G. Pettifor, Theoretical predictions of structure and related properties of intermetallics, *Mater. Sci. Technol.*, 1992, **8**(4), 345–349.

54 S. F. Pugh, XCII. Relations between the elastic moduli and the plastic properties of polycrystalline pure metals, *London, Edinburgh Dublin Philos. Mag. J. Sci.*, 1954, **45**(367), 823–843.

55 I. N. Frantsevich, *Elastic constants and elastic moduli of metals and insulators*, Ref. B., 1982.